

SMA OBSERVATIONS OF W3(OH) COMPLEX: PHYSICAL AND CHEMICAL DIFFERENTIATION BETWEEN W3(H₂O) AND W3(OH)

SHENG-LI QIN,¹ PETER SCHILKE,² JINGWEN WU,³ YUEFANG WU,⁴ TIE LIU,⁵ YING LIU,⁶ ÁLVARO SÁNCHEZ-MONGE²

ABSTRACT

We report on the Submillimeter Array (SMA) observations of molecular lines at 270 GHz toward W3(OH) and W3(H₂O) complex. Although previous observations already resolved the W3(H₂O) into two or three sub-components, the physical and chemical properties of the two sources are not well constrained. Our SMA observations clearly resolved W3(OH) and W3(H₂O) continuum cores. Taking the advantage of the line fitting tool XCLASS, we identified and modeled a rich molecular spectrum in this complex, including multiple CH₃CN and CH₃OH transitions in both cores. HDO, C₂H₅CN, O¹³CS, and vibrationally excited lines of HCN, CH₃CN, and CH₃OCHO were only detected in W3(H₂O). We calculate gas temperatures and column densities for both cores. The results show that W3(H₂O) has higher gas temperatures, and larger column densities than W3(OH) as previously observed, suggesting physical and chemical differences between the two cores. We compare the molecular abundances in W3(H₂O) to those in the Sgr B2(N) hot core, the Orion KL hot core and the Orion Compact Ridge, and discuss the chemical origin of specific species. An east-west velocity gradient is seen in W3(H₂O), and the extension is consistent with the bipolar outflow orientation traced by water masers and radio jets. A north-south velocity gradient across W3(OH) is also observed. However, with current observations

¹Department of Astronomy, Yunnan University, and Key Laboratory of Astroparticle Physics of Yunnan Province, Kunming, 650091, China; slqin@bao.ac.cn

²Physikalisches Institut, Universität zu Köln, Zùlpicher Str. 77, D-50937 Köln, Germany

³Department of Physics and Astronomy, University of California, Los Angeles, CA 90095, USA

⁴Department of Astronomy, Peking University, Beijing, 100871, China

⁵Korea Astronomy and Space Science Institute 776, Daedeokdaero, Yuseong-gu, Daejeon, Republic of Korea 305-348

⁶Department of Physics and Hebei Advanced Thin Film Laboratory, Hebei Normal University, Shijiazhuang 050024, China

we can not assure if the velocity gradients are caused by rotation, outflow or radial velocity differences of the sub-components in W3(OH).

Subject headings: ISM:abundances — ISM: individual (W3(OH)) — ISM: molecules — radio lines: ISM — star: formation

1. INTRODUCTION

How massive stars form is poorly understood yet, partly because powerful radiation pressure from stars with masses above $\sim 8 M_{\odot}$ should prevent the gas accretion on the protostars to form more massive stars, according to the monolithic collapse model. Different theoretical scenarios related to high-mass star formation have been proposed, i.e., monolithic collapse (e.g., Jijina & Adams 1996; McKee & Tan 2003), competitive accretion and coalescence (e.g., Bonnell et al. 1997, 1998), and how each of them takes effects depends on the initial environments of their parent clouds (Zinnecker & Yorke 2007, Tan et al. 2014). Observations are essential to test scenarios of high-mass star formation. Lower spatial resolution observations can not resolve detailed structure due to their large distances, nor can they explore the clustered environments, and small scale variations in high-mass star forming regions. Higher spatial resolution observations are necessary to characterize kinematics, physical and chemical conditions of high-mass star forming regions at small spatial scales.

The W3(OH) complex, located at 2.04 kpc (Hachisuka et al. 2006), is one of the nearest and well-studied high-mass star forming regions, and harbors two objects, W3(OH) and W3(H₂O). Radio observations suggested that W3(OH) is an UC HII region, ionized by young OB stars, and is rich in OH masers (Reid et al. 1995; Wilner et al. 1999; Fish & Sjouwerman 2007). W3(H₂O), also known as W3(OH)-TW (Turner & Welch 1984), locates 6'' east of W3(OH) and is rich in H₂O maser and organic molecules (Wyrowski et al. 1999; Chen et al. 2006; Zapata et al. 2011; Hernández-Hernández et al. 2014), and presents hot core properties (Kurtz et al. 2000). Single dish observations have shown overall inflow in the W3(OH) complex (Wu & Evans 2003), and outflows as well as a possible disk were identified by Zapata et al. (2011). Subarcsec resolution observations of continuum and CH₃CN lines showed a high-mass protobinary system in W3(H₂O), with the two sub-cores having different physical properties (Chen et al. 2006). However, physical and chemical properties of W3(H₂O) and W3(OH) are still not well characterized.

In this paper, we present results from Submillimeter Array (SMA¹) observations towards

¹The Submillimeter Array is a joint project between the Smithsonian Astrophysical Observatory and the

the W3(OH) complex with moderate spatial resolution. Our goal is to study the physical and chemical differences between W3(H₂O) and W3(OH). The observations were tuned to 267 GHz covering the linear molecule HCN and other complex molecules. Compared to other submillimeter bands, molecular emissions at 267 GHz have less line confusion (Greaves & White 1991). We describe the observations in §2. In §3 we present the spectral line results, followed by data analysis in §4. §5 discusses differences of physics and chemistry of the two sources. We summarize the results in §6.

2. OBSERVATIONS

The track-sharing SMA observations were carried out with seven antennas on 2007, November 30, in its compact array, for a total of 10.23 hours on calibrators and the target sources (W3(OH) and S231). The phase-tracking center of the W3(OH) complex was at R.A.=02^h27^m04^s.68, decl.=+61°52′25″.5 (J2000.0). The database covers 4 GHz bandwidth, ranging from 265.65 to 267.65 GHz (lower sideband), and from 275.65 to 277.65 GHz (upper sideband). The frequency resolution of 0.406 MHz corresponds to a velocity resolution of ~ 0.5 km s^{−1}. The average zenith opacity ($\tau_{225\text{GHz}}$) measured by the tipping radiometer at the Caltech Submillimeter Observatory (CSO) was 0.12, indicating moderate weather conditions during observations. Uranus (~ 45 Jy at 1.1 mm band) was observed for bandpass calibration. The QSOs 0136+478 (~ 1.8 Jy) and 3c111 (~ 7.2 Jy) were observed in the ascending time order, for phase correction. Flux calibration is based on observations of Uranus and a model of its brightness distribution. Comparing with flux derived from the quasar monitoring, the flux calibration is estimated to be accurate to within 20%.

The data were calibrated and imaged in Miriad (Sault, Teuben & Wright 1995). We selected line-free channels for continuum-subtraction in the (u, v) domain using the UVLIN task. The projected baselines ranged from 8 to 64 k λ . The resulting synthesized beam is $\sim 2''.7 \times 2''.4$ (PA=−61°). The continuum image was obtained by averaging all line-free channels of the lower and upper sidebands resulting in a sensitivity of 0.02 Jy beam^{−1}. The 1 σ noise level of the spectral line images is 0.1 Jy beam^{−1} per channel. 1 Jy beam^{−1} in these observations corresponds to a main beam brightness temperature of ~ 2.4 K.

3. RESULTS

3.1. *Continuum*

Figure 1 presents the synthesized 1.1 mm continuum image, in which the two cores, W3(H₂O) and W3(OH), are well resolved. The peak intensity, total flux density, and deconvolved source size from a 2D Gaussian fit to the two continuum cores are summarized in Table 1. W3(H₂O) and W3(OH) have comparable peak intensities, but different flux densities and source sizes. The dust mass and source-averaged H₂ column density of W3(H₂O) can be calculated by the formulae (Hildebrand 1983)

$$M_{\text{gas}} = \frac{S_{\nu} D^2 R}{\kappa_{\nu} B_{\nu}(T)}, \quad (1)$$

$$N(\text{H}_2) = \frac{S_{\nu} R}{2m_H \Omega \kappa_{\nu} B_{\nu}(T)}, \quad (2)$$

where S_{ν} is the continuum flux, D is the distance to source, R is the gas-to-dust ratio (100), Ω is the solid angle subtended by the source, and $B_{\nu}(T)$ is the Planck function at temperature T . The dust mass opacity coefficient κ_{ν} of 1.55 cm² g⁻¹ is interpolated from the values of no-coagulated dust grains with thin ice mantles (Ossenkopf & Henning 1994). A dust temperature of 100 K is adopted for the W3(H₂O) core (Chen et al. 2006; Zapata et al. 2011). The derived H₂ column density and mass (listed in Table 1) are slightly larger than those derived by Hernández-Hernández et al. (2014), probably due to the lower angular resolution of our observations that allow us to recover more extended emission. The continuum source that we detect at the position of W3(OH) is mainly free-free emission from the HII region associated with it (Willner et al. 1995; Wyrowski et al. 1997, 1999). An upper limit of 0.5 Jy at 220 GHz is inferred from dust emission (Wyrowski et al. 1999). Therefore, our continuum observations can not provide a reliable estimation for the H₂ column density towards W3(OH).

3.2. *Molecular lines*

We identify line transitions using XCLASS² package. XCLASS accesses the CDMS (Müller et al. 2001, 2005; <http://www.cdms.de>) and JPL (Pickett et al. 1998; <http://spec.jpl.nasa.gov>)

²<http://www.astro.uni-koeln.de/projects/schilke/XCLASS>

molecular databases which provide all necessary spectroscopic information: rest frequency, integrated intensity, lower state energy, upper state degeneracy, quantum numbers and the partition function. Figure 2(a) and (b) show the lower and upper sideband spectra extracted from the image domain in both cores W3(H₂O) and W3(OH), with the different line identifications. At a first glance, there are more lines in W3(H₂O) than in W3(OH). Strong emission of rotational transitions of HCN, HCO⁺, OCS, ¹³CS, CH₃OH, CH₃OCHO and CH₃CN as well as highly excited CH₃OH transitions are present in both cores. While vibrationally excited lines HCN $v_2=1$, CH₃OCHO $v=1$, CH₃CN $v_8=1$, as well as rotational transitions of C₂H₅CN, HDO, CH₂NH, O¹³CS are only detected in W3(H₂O). The CH₃OH rotational transitions in W3(OH) have higher intensities than in W3(H₂O), while the vibrational lines appear stronger in W3(H₂O). Note that five CH₃¹³CN transitions were detected only in W3(H₂O) (see Figure 2(c) for an enlarged version). The spectral differences between W3(OH) and W3(H₂O) are probably caused by excitation conditions or molecular abundances, in which W3(H₂O) has hotter gas environments and higher abundances than W3(OH) (Hernández-Hernández et al. 2014; also see discussion in sections 4.1 and 4.2). The H₄₀ γ recombination line at 276.746 GHz is observed in W3(OH), but not in W3(H₂O), confirming the presence of a bright HII region in W3(OH).

3.3. *Gas distribution*

Previous higher spatial resolution continuum observations already resolved W3(H₂O) into three sub-components: A, B and C (Wyrowski et al. 1999). The line observations suggest that nitrogen-bearing molecules only peak at component C and oxygen-bearing molecules have a different distribution (Wyrowski et al. 1999). Figure 3 presents maps of different molecular species. C₂H₅CN and HCN vibrational transitions are only detected towards W3(H₂O). While CH₃CN, CH₃OCHO, and higher energy CH₃OH (at 266.704 GHz) transitions are present in both cores, with higher intensities observed towards W3(H₂O). The morphology of CH₃OH at 266.838 GHz is almost the same as the continuum image (see Figure 1) which may indicate its grain surface origin. The line emission and gas distribution indicate different physical and chemical conditions for the two sources.

3.4. *Velocity structure*

The line velocities generally trace kinematics in molecular clouds. Mean systematic velocities of -49.4 and -45.1 km s⁻¹ for W3(H₂O) and W3(OH) are obtained from modeling of various molecular lines (see Table 2 and next section), which is roughly consistent with

the values derived from CH_3CN lines by Hernández-Hernández et al. (2014). The systematic velocity variations among the different species are also observed in $\text{W3(H}_2\text{O)}$, which are likely caused by the chemical differences of the molecules at a small scale. High spatial resolution observations of CH_3CN lines resolve the A and C components in $\text{W3(H}_2\text{O)}$ and reveal different systematic velocities of -51.4 and -48.6 km s^{-1} (Chen et al. 2006). Systematic velocities of -50.5 and -46.5 km s^{-1} for the A and C components are derived by Zapata et al. (2011). In our SMA observations, $\text{HCN } v_2=1$ and $\text{C}_2\text{H}_5\text{CN}$ appear to peak at the same position, and have a systemic velocity (-48.5 km s^{-1}) similar to that of component C. While CH_3CN , CH_3OH and CH_3OCHO peak at a different positions, and have a systemic velocity -49.6 km s^{-1} , which is not consistent with that of components A or C. Future observations of various species with higher spatial, spectral resolution, and better sensitivity can resolve the detailed structure, and make an overall physical and chemical picture of this high-mass star formation region.

In order to display the detailed velocity structure and kinematics, we present velocity channel maps of $\text{HCN } v_2=1$ at 267.199 GHz and the lower energy level CH_3OH rotational transition at 266.838 GHz in Figure 4. In addition to the compact gas emission concentrated on the continuum peak around the systematic velocity, the $\text{HCN } v_2=1$ blue-shifted emission with velocity ranging from -54 to -50 km s^{-1} locates to the east of the $\text{W3(H}_2\text{O)}$ continuum peak, while red-shifted emission from -46 to -42 km s^{-1} is located west of the $\text{W3(H}_2\text{O)}$ continuum peak. The east-west velocity gradient across $\text{W3(H}_2\text{O)}$ is also seen in intensity-weighted velocity map (moment 1) of $\text{HCN } v_2=1$ line, as shown in the left panel of Figure 5. There is no $\text{HCN } v_2=1$ emission towards W3(OH) . The blue-shifted feature in $\text{W3(H}_2\text{O)}$ is also seen in lower energy CH_3OH transition. The velocity gradient seen in the east-west direction was also reported using other molecular tracers (Wyrowski et al. 1997; Chen et al. 2006), and is consistent with the outflow orientation traced by water masers and radio jets (Alcolea et al. 1993; Wilner et al. 1995). Additionally, a north-south velocity gradient in W3(OH) is observed in the CH_3OH channel maps of Figure 4, covering a velocity range from -48 to -41 km s^{-1} . The first order moment image of CH_3OH is shown in the right panel Figure 5, and it reveals the systemic velocity difference between $\text{W3(H}_2\text{O)}$ and W3(OH) . However, whether the velocity gradient is caused by outflow, disk, radial velocity differences of multiple sources, or binary rotation is still unclear. Higher spatial and spectral resolution observations of multiple lines are needed to explain the velocity gradient.

4. ANALYSIS

4.1. *Rotation temperature and column density*

The rotation temperature diagram (RTD) method based on multi-transition observations is commonly used for determining physical parameters, in which population distribution of all energy levels of a specific species is described by a single excitation temperature and column density (Goldsmith & Langer 1999). RTD can be safely used in an homogeneous cloud with simple spectral profiles, optically thin emission, and a large spatial extension that completely covers the observing beam. However perfect homogeneous clouds are not observed in interstellar space, and complex density and temperature structures have been observed even in clouds with a simple morphology. Under assumption of local thermodynamical equilibrium (LTE), the XCLASS program solves for the radiative transfer equation which takes source size, beam filling factor, line profile, line blending, background temperature, excitation, and opacity into account. The main difference between RTD and XCLASS fitting is that XCLASS can deal with opacity, line blending, and multiple velocity and spatial components. The detailed fitting functions and modeling procedures are described in the papers by Comito et al. (2005) and Zernickel et al. (2012). The source sizes are derived by two dimensional Gaussian fitting to the individual spatial components and converted to circular sizes. Then, LTE modeling is performed on the observed spectrum (see Figure 2). The systemic velocities, line widths, rotation temperatures and column densities of observed species derived with XCLASS modeling are listed in Table 2. The results show that different molecules have different rotational temperatures and column densities. The differences in the physical (distribution in the cloud) and chemical properties of the different molecules explain why not a single temperature is observed for all the species (see review by van Dishoeck & Blake 1998).

Note that in Figure 2C, the predicted intensities for the lines with optical depths larger than 1 are stronger than those in the observed spectra, while the predicted intensities for the lines with optical depths less than 1 are coincident with the observed ones. For the optically thick transitions, one just sees the $\tau=1$ surface due to photon trapping, while the XCLASS models sum up all the contributions from the cloud linearly.

Multiple transitions of CH_3CN and CH_3OH spanning a wide energy range (the upper level energies are labelled in Figure 2) are observed in both W3(H₂O) and W3(OH), which can provide constraints on parameter estimation, especially for gas temperatures. In principle, the higher energy transitions will sample the emission from hot cores since these transitions are populated in conditions of high densities and temperatures, while the lower energy transitions can be excited in both the warm and the cool surrounding regions. There-

fore two components with different temperatures and column densities are needed to model CH₃CN and CH₃OH in the line abundant region W3(H₂O). We discuss individual molecules in the following.

CH₃CN is thought to be a good probe of kinetic temperature of high density gas (e.g., Remijan et al. 2004; Schilke et al. 1997). Seven CH₃CN rotational transitions (with E_u of 105–363 K) are detected in W3(H₂O). The rotational transitions of CH₃CN in W3(H₂O) can not be fitted by a single gas temperature, two component modeling with gas temperatures of 55 (cold) and 200 K (warm), and column densities of 0.15×10^{17} and 0.3×10^{17} cm⁻² are needed. Five CH₃¹³CN transitions were also observed in W3(H₂O), of which three are blended with CH₃CN. Using the same temperatures as for CH₃CN, the derived column densities are 0.002×10^{17} and 0.004×10^{17} cm⁻² for the warm and cold components, respectively. Six CH₃CN $v_8=1$ vibrational lines (with E_u of 625–692 K) are detected towards W3(H₂O). The LTE modeling of the CH₃CN $v_8=1$ gives a rotation temperature of 200 K and a column density of 0.3×10^{17} cm⁻². The rotational transitions of CH₃CN are also detected in W3(OH), but have lower intensities than in W3(H₂O). No CH₃CN $v_8=1$ or CH₃¹³CN are detected in this core. The observed spectra can be fitted by a single gas temperature of 95 K and column density of 0.016×10^{17} cm⁻², which are lower than in W3(H₂O).

Three C₂H₅CN spectral features were identified toward W3(H₂O), but not in W3(OH). A rotation temperature of 105 K and column density of 0.08×10^{17} cm⁻² were derived.

One rotational transition of HCN was detected in both cores showing complicated kinematics (infall and outflow profiles that are discussed in Qin et al. 2015). Two vibrationally excited HCN transitions (with E_u of 1050 K) have been only detected in W3(H₂O), giving a rotation temperature of 360 K and column density of 0.25×10^{17} cm⁻².

CH₃OH has been widely detected in various star-forming regions. Four rotational transitions (with E_u of 57–690 K) and one vibrational transition (with E_u of 710 K) were detected in both cores, but high energy transition in W3(H₂O) have higher intensities than in W3(OH), while a higher intensity for the lower energy transitions is observed in W3(OH). Similar to CH₃CN, a two temperature component model is needed, giving rotation temperatures of 55 and 360 K, a column densities of 2.4×10^{17} and 5.5×10^{17} cm⁻² in W3(H₂O). One temperature component fit to W3(OH) gives a gas temperature of 155 K, and a slightly lower column density compared with W3(H₂O).

Nine weak spectral features of CH₃OCHO (with E_u of 351–365 K) were identified in its vibrational state, and one rotational transition (with E_u of 160 K) was detected in W3(H₂O). Only one rotational transition was detected in W3(OH). The derived rotation temperature and column density are 105 K and 1.1×10^{17} cm⁻² toward W3(H₂O).

The molecules with only one transition detected are HDO, CH₂NH, O¹³CS, OCS, SO₂, and ¹³CS. Note that HDO, CH₂NH and O¹³CS were only detected towards W3(H₂O), and CH₂NH was marginally detected. They have similar morphologies to the other species detected in W3(H₂O) or W3(OH). Assuming excitation temperatures of 105 K and 95 K for W3(H₂O) and W3(OH), we derived the column densities for these molecules (see Table 2).

4.2. Abundance

The column density of a specific molecule is related to its opacity. Chemical models use the fractional abundance of a molecule relative to H₂. We derived the fractional abundances of the observed molecules relative to H₂ by $f_{\text{H}_2} = N_T/N_{\text{H}_2}$ (see Table 2), where N_T is the total column density of a specific molecule and N_{H_2} is the H₂ column density derived from the continuum. Since no reliable H₂ column density is available for W3(OH), we only calculate fractional abundances of molecules in W3(H₂O). They are compared to other star forming regions in section 5.2. In general, molecules in W3(H₂O) with a small source size have a high gas temperature and fractional abundance. The observations of multiple CH₃CN transitions toward a sample of hot cores showed that the sources with high gas temperatures have larger fractional abundances (Hernández-Hernández et al 2014). These results will provide important constraints on chemical models.

4.3. Isotopic ratio

Both CH₃CN and CH₃¹³CN were observed in W3(H₂O), which is useful for demonstrating the line blending and opacity effects in the modeling calculation. The close-up view of the CH₃CN and CH₃¹³CN modeling is shown in Figure 2(c), in which red and green curves are the synthetic spectra of CH₃CN and CH₃¹³CN, respectively, using both warm (200 K) and cold (55 K) components, and the calculated opacity is shown in lower panel. The high energy transitions of CH₃CN tend to be optically thin, and opacities of CH₃¹³CN transitions are much lower than those of CH₃CN. The two component modeling results suggested that W3(H₂O) has an inner structure that is unresolved in these observations. The rotation temperature of 200 K for the warm component is consistent with that measured with HNC lines (Wyrowski et al. 1999). A ratio for ¹²C/¹³C of 75 is obtained from the derived column density of CH₃CN and its isotopologues (see Table 2), which is consistent with the value of 76±7 determined by Henkel, Wilson & Bieging (1982).

The peak optical depth can also be estimated from the observed intensity ratio of CH₃CN

and $\text{CH}_3^{13}\text{CN}$ as $\frac{T_{\text{mb}}(\text{CH}_3\text{CN})}{T_{\text{mb}}(\text{CH}_3^{13}\text{CN})} \sim \frac{1-e^{-\tau(\text{CH}_3\text{CN})}}{1-e^{-\tau(\text{CH}_3\text{CN})/R}}$, where R is $^{12}\text{C}/^{13}\text{C}$ ratio. The observed peak intensities of CH_3CN ($15_2 - 14_2$) and $\text{CH}_3^{13}\text{CN}$ ($15_2 - 14_2$) are 16.7 and 1.7 K, respectively. Taking $^{12}\text{C}/^{13}\text{C}$ to be 76, we derive an optical depth of 7.7 for CH_3CN ($15_2 - 14_2$) which is roughly consistent with that determined from the XCLASS modeling (See Figure 2(C)).

5. DISCUSSION

5.1. *Detection and non-detection of species*

We now discuss the detection and non-detection of some species in the W3(OH) complex. High and low excitation lines of CH_3OH have been detected in both $\text{W3(H}_2\text{O)}$ and W3(OH) , but the transition with the lowest energy level (at 266.838 GHz) in W3(OH) has a larger extension and higher intensity than in $\text{W3(H}_2\text{O)}$, indicating a lower excitation condition in W3(OH) . The most abundant species in these observations is CH_3OH . Vibrationally excited lines of $\text{HCN } v_2=1$, $\text{CH}_3\text{OCHO } v=1$, $\text{CH}_3\text{CN } v_8=1$, and rotational transitions of $\text{C}_2\text{H}_5\text{CN}$, HDO , CH_2NH , O^{13}CS are only detected in $\text{W3(H}_2\text{O)}$, and they have lower abundances when compared to CH_3OH . Probably the lower abundances make these transitions too weak in W3(OH) , and the expected intensities are lower than the SMA detection limit. We take O^{13}CS as an example to test this assumption. In $\text{W3(H}_2\text{O)}$, the column density ratio of OCS and O^{13}CS is 80 (See Table 2). The column density of OCS in W3(OH) is $0.25 \times 10^{17} \text{ cm}^{-2}$. Assuming that OCS and O^{13}CS in W3(OH) have the same source size, gas temperature, and a column density ratio of 80, we simulated O^{13}CS emission using XCLASS, and the predicted O^{13}CS intensity is much lower than the 1σ detection limit of our SMA observations. Therefore we argue that the detection and non-detection of some species indeed reflect physical and chemical differences between $\text{W3(H}_2\text{O)}$ and W3(OH) .

5.2. *Individual species*

Three regions: the Sgr B2(N) hot core, the Orion KL hot core and Orion Compact Ridge, have the richest line emission in our Galaxy, and are good targets with which compare our results. In our observations towards $\text{W3(H}_2\text{O)}$, the species CH_3OH , CH_3CN and CH_3OCHO , are detected in more than three transitions. In Figure 6, we show the abundances of the three species relative to H_2 , compared to Herschel/HIFI observations of the Sgr B2(N) hot core (Neill et al. 2014), the Orion KL hot core and Compact Ridge (Crockett et al. 2014). The comparison is reasonable, since the results of the Sgr B2(N) and Orion KL presented in Neill et al. (2014) and Crockett et al. (2014), and the results of $\text{W3(H}_2\text{O)}$ presented in this

work, have been obtained using the same tool, XCLASS. A possible source of uncertainty is the adopted H_2 column density. The abundances among the four sources are similar, suggesting that these molecules have a same chemical origin in W3(H_2O) as in the Orion KL and Sgr B2(N) sources, i.e., they originate from warm gas environments where some species are released from grain surfaces and involved into the gas phase chemistry. We discuss these molecules in the following.

The derived rotation temperatures for CH_3OH in W3(H_2O) suggest that there are cold and hot gas components, and the higher gas temperature component has a larger fractional abundance. Laboratory works also confirmed that some complex species with higher gas temperatures also have larger abundances (Fortman et al. 2010, 2014). Compared with other organic species in these observations, CH_3OH has the highest fractional abundance. Similar cases are also reported in other star forming regions (e.g., Ge et al. 2014; van der Tak, van Dishoeck & Caselli 2000; Qin et al. 2010; Crockett et al. 2014; Neill et al. 2014). Infrared observations suggest that CH_3OH is the second most abundant ice species and has the highest abundance relevant to water ice with a fraction of 5–30% (e.g., Dartois et al. 1999). The high abundance of CH_3OH indicates that this species may originate from grain surface chemistry (Charnely et al. 2004; Garrod & Herbst 2006). The morphology of the lower energy CH_3OH transition at 266.838 GHz is almost the same as the continuum emission, which provides another support for the grain surface origin of CH_3OH . CH_3OCHO is detected in the Herschel/HIFI survey of the Compact Ridge, but not in the Orion KL hot core and Sgr B2(N) (Crockett et al. 2014; Neill et al. 2014). This molecule may derive from CH_3OH on grain surface (Garrod & Herbst 2006) or in the gas phase (Laas et al. 2011).

Both rotational and vibrational transitions of CH_3CN were detected in W3(H_2O). The derived rotation temperature of 200 K for the warm component is consistent with that obtained by Wyrowski et al. (1999). The warm component has a higher fractional abundance than the cold component, which is consistent with the trend that abundance increases with rotation temperature derived by Hernández-Hernández et al. (2014). Also, a similar abundance is measured in the Orion KL and Sgr B2(N). These facts support that CH_3CN is synthesized by high temperature gas phase reactions (Hernández-Hernández et al. 2014; Neill et al. 2014). There is no detection of CH_3CN vibrational transitions in W3(OH). The intensities of rotational transitions of CH_3CN in W3(OH) are much lower than those in W3(H_2O), too. The derived column density is one order of magnitude lower than that in W3(H_2O).

The HDO transition at 266.161 GHz has been detected in the OMC1 cloud (Greaves & White 1991). HDO was only detected in W3(H_2O) in our SMA observations. An HDO abundance relative to H_2 of 1.5×10^{-8} is derived. As stated above, CH_3OH may originate from

grain surface chemistry. If taking the abundance of CH_3OH relative to water as 10%, one obtains $\text{HDO}/\text{H}_2\text{O}=1.6\times 10^{-2}$, which may indicate that W3(H_2O) is at an early evolutionary stage (Miettinen, Hennmann & Linz 2011).

5.3. Chemical difference between W3(H_2O) and W3(OH)

There are more lines in W3(H_2O) than in W3(OH). Furthermore, for the same species, higher gas temperatures and column densities are obtained in W3(H_2O), which indeed reflects different physics and chemistry between the two sources. The differences may come from the fact that W3(H_2O) is at an early evolutionary stage of high-mass star formation (e.g., Wyrowski et al. 1999; Chen et al. 2006), while W3(OH) is an expanding shell-like H II region (Dreher & Welch 1981; Kawamura & Masson 1998). The central star in W3(OH) is optically obscured by a dusty cocoon (Wynn-Williams et al. 1972). Therefore the gas seen in W3(OH) probably comes from the outer region of the hot core that evolved into the UC HII region, and the inner portion of this hot core has been dissociated and ionized by the stars.

6. SUMMARY

1. To characterize the physical and chemical differences between W3(H_2O) and W3(OH), we have carried out high spatial resolution multi-line observations with the SMA at 270 GHz. The SMA observations clearly resolved the two sources, W3(H_2O) and W3(OH) continuum cores. More lines are detected in W3(H_2O) than in W3(OH). Rotational transitions of CH_3OH , CH_3OCHO and CH_3CN are detected in both cores. While vibrationally excited lines of $\text{HCN } v_2=1$, $\text{CH}_3\text{OCHO } v=1$, $\text{CH}_3\text{CN } v_8=1$, and rotational transitions of $\text{C}_2\text{H}_5\text{CN}$, HDO are only detected in W3(H_2O). These features confirm that W3(H_2O) does present hot core properties.

2. We have modeled the observed molecular lines using the XCLASS software, under the assumption of LTE, and taking into account the source size, beam filling factor, line profile, line blending, background temperature, and excitation effects. Rotation temperatures, column densities and fractional abundances are derived. Generally, the rotation temperatures and column densities are higher in W3(H_2O) than in W3(OH). These properties indeed reflect physical and chemical differences between the two sources. The differences are caused by the fact that W3(H_2O) is a hot core, while the gas seen in W3(OH) seems to come from the outer region of the hot cores located outside of the H II region.

3. The abundances of CH_3OH , CH_3OCHO and CH_3CN in W3(H_2O) is similar with those in the Sgr B2(N) hot core, the Orion KL hot core and Compact Ridge, suggesting that these molecules have similar chemical origins. Among the molecules detected, CH_3OH has the highest gas abundance, and the morphology of its lowest energy transition is coincident with that of the continuum, suggesting that it likely originates from grain surface chemistry. The abundance of CH_3CN increases as temperature rises, and probably CH_3CN was synthesized in high temperature gas phase reactions. Non-detection and detection of some species such as HDO, O^{13}CS , $\text{C}_2\text{H}_5\text{CN}$ in the two cores may be related to their molecular abundance or evolution. Vibrationally excited HCN and CH_3CN were detected in W3(H_2O), but not in W3(OH); this is probably due to hot core environment of the W3(H_2O). The estimated HDO abundance relative to H_2O in W3(H_2O) is $\sim 1.6 \times 10^{-2}$, indicating an early evolutionary stage.

4. Spectral images showed compact source structure centered at W3(H_2O) or W3(OH). The velocity channel maps of HCN $v_2=1$ and CH_3OH show a east-west velocity gradient in W3(H_2O) which is consistent with the outflow orientation traced by water masers and radio jets. A north-south velocity gradient is seen in W3(OH).

We thank the anonymous referee for his/her constructive comments on the paper. This work has been supported by the National Natural Science Foundation of China under grant Nos. 11373026, 11373009, 11433004, 11433008, U1331116, and the National Basic Research Program of China (973 Program) under grant No. 2012CB821800, by Top Talents Program of Yunnan Province and Midwest universities comprehensive strength promotion project (XT412001, Yunnan university), by the Deutsche Forschungsgemeinschaft, DFG through project number SFB956.

REFERENCES

- Alcolea, J., Menten, K. M., Moran, J. M., & Reid, M. J. 1993, in Proc. Conf. Astrophysical masers, ed. A. W. Clegg & G. E. Nedoluha (New York: Springer), Vol. 412, 225
- Bonnell, I. A., Bate, M. R., Clarke C. J, & Pringle J. E. 1997, MNRAS, 285, 201
- Bonnell, I. A., Bate, M. R., & Zinnecker, H. 1998, MNRAS, 298, 93
- Charnley, S. B., Ehrenfreund, P., Millar, T. J., et al. 2004, MNRAS, 347, 157
- Chen, H.-R., Welch, W. J., Wilner, D. J., & Sutton, E. C. 2006, ApJ, 639, 975
- Comito, C., Schilke, P., Phillips, T. G., et al. 2005, ApJS, 156, 127
- Crockett, N., Bergin, E., Neill, J., et al. 2014, ApJ, 787, 112
- Dartois, E., Schutte, W., Geballe, T. R., et al. 1999, A&A, 342, L32
- Dreher, J.W., & Welch, W. J. 1981, ApJ, 245, 857
- Fish, V. L., & Sjouwerman, L. O. 2007, ApJ, 668, 331
- Fortman, S. M., Medvedev, I. R., Neese, C., & De Lucia, F. C. 2010, ApJ, 725, L11
- Fortman, S. M., Neese, C., & De Lucia, F. C. 2014, ApJ, 782, 75
- Garrod, R. T., & Herbst, E. 2006, A&A, 457, 927
- Ge, J. X., He, J. H., Chen, X., & Takahashi, T. 2004, MNRAS, 445, 1170
- Greaves, J. S., & White, G. J. 1991, A&AS, 91, 237
- Goldsmith, P. F., & Langer, W. D. 1999, ApJ, 517, 209
- Hachisuka, K., Brunthaler, A., Menten, K. M., et al. 2006, ApJ, 645, 337
- Henkel, C., Wilson, T. L., & Bieging, J. 1982, A&A, 109, 344
- Hernández-Hernández, V., Zapata, L., Kurtz, S., & Garay, G. 2014, ApJ, 786, 38
- Hildebrand, R. H. 1983, QJRAS, 24, 267
- Jijina, J., & Adams, F. C. 1996, ApJ, 462, 874
- Kawamura, J. H., & Masson, C. R. 1998, ApJ, 509, 270

- Kurtz, S., Cesaroni, R., Churchwell, E., Hofner, P., & Walmsley, C. M. 2000, in *Protostars & Planets IV*, ed. V. Mannings, A. Boss & S. Russell (Tucson: Univ. Arizona Press), 299
- Lass, J., Gorrod, R., Herbst, E., & Weaver, S. W. 2011, *ApJ*, 728, 71
- McKee, C. F., & Tan, J. C. 2003, *ApJ*, 585, 850
- Miettinen, O., Hennemann, M., & Linz, H. 2011, *A&A*, 534, 134
- Müller, H. S. P., Thorwirth, S., Roth, D. A., & Winnewisser, G., 2001, *A&A*, 370, L49
- Müller, H. S. P., Schlöder, F., Stutzki, J., & Winnewisser, G. 2005, *JMoSt*, 742, 215
- Neill, J., Bergin, E., Lis, D., et al. 2014, *ApJ*, 789, 8
- Ossenkopf, V., & Henning, T. 1994, *A&A*, 291, 943
- Pickett, H. M., Poynter, R. L., Cohen, E. M., et al. 1998, *JQSRT*, 60, 883
- Qin, S.-L., Wu, Y. F., Huang, M. H., et al. 2010, *ApJ*, 711, 399
- Qin, S.-L., Schilke, P., Wu, J. W., et al. 2015, submitted to *ApJ Letters*
- Reid, M. J., Argon, A. L., Masson, C. R., et al. 1995, *ApJ*, 443, 238
- Remijan, A., Sutton, E. C., Snyder, L. E., et al. 2004, *ApJ*, 606, 917
- Sault, R. J., Teuben, P. J., & Wright, M. C. H. 1995, in *Astronomical Data Analysis Software and Systems IV*, ed. R. A. Shaw, H. E. Payne, & J. J. E. Hayes (San Francisco, CA: ASP), ASP Conf. Ser., 77, 433
- Schilke, P., Groesbeck, T. D., Blake, G. A., & Phillips, T. G. 1997, *ApJS*, 108, 301
- Tan, J. C., Beltrán, M. T., Caselli, P., Fontani, F., Fuente, A., Krumholz, M. R., McKee, C. F., & Stolte, A. 2014, in *Protostars and Planets VI*, ed. H. Beuther, R. S. Klessen, C. P. Dullemond, & T. Henning (Tucson: Univ. Arizona Press), 914, 149
- Turner, J. L., & Welch, W. J. 1984, *ApJ*, 287, L81
- van der Tak, F. F. S., van Dishoeck, E. F., & Caselli, P. 2000, *A&A*, 361, 327
- van Dishoeck, E. F., & Blake, G. A. 1998, *ARA&A*, 36, 317
- Wilner, D. J., Welch, W. J., & Forster, J. R. 1995, *ApJ*, 449, L73

- Wilner, D. J., Reid, M. J., & Menten, K. M. 1999, *ApJ*, 513, 755
- Wu, J. W., & Evans II, N. J. 2003, *ApJ*, 592, L79
- Wynn-Williams, C. G., Becklin, E. E., & Neugebauer, G. 1972, *MNRAS*, 160, 1
- Wyrowski, F., Hofner, P., Schilke, P., et al. 1997, *A&A*, 320, L17
- Wyrowski, F., Schilke, P., Walmsley, C. M., & Menten, K. M. 1999, *ApJ*, 514, L43
- Zapata, L. A., Rodríguez-Garza, C., Rodríguez, L.F., et al. 2011, *ApJ*, 740, L19
- Zernickel, A., Schilke, P., Schmiedeke, A., et al. 2012, *A&A*, 546, 87
- Zinnecker, H., & Yorke, H. W. 2007, *ARA&A*, 45, 481

Table 1. Physical Parameters Of the Continuum Sources

Name	Δ R.A. "	Δ decl "	I_{peak} Jy beam ⁻¹	S_{ν} Jy	Deconvolved Angular Size "	N_{H_2} cm ⁻²	Mass (M _⊙)
W3(H ₂ O)	-0.5	-0.8	2.25±0.14	4.6±0.3	3.4×1.9 (-72.5°)	2.6×10 ²⁴	26
W3(OH)	-5.9	-0.9	2.28±0.18	3.8±0.3	2.5×1.6 (73.4°)

Note: The offset positions are relative to phase track center of the observations at R.A.=02^h27^m04^s.68, decl.=+61°52′25″.5 (J2000.0).

Table 2. The Parameters Derived From Molecular Lines

Molecule	Θ "	T_{rot} (K)	N_T (cm ⁻²)	f_{H_2}	V_{LSR} (km s ⁻¹)	ΔV (km s ⁻¹)
W3(H ₂ O)						
CH ₃ OH	2.86	55	2.4×10 ¹⁷	9.2×10 ⁻⁸	-49.6	7
	0.9	360	5.5×10 ¹⁷	2.1×10 ⁻⁷	-50.6	4
CH ₃ OCHO	2.33	105	1.1×10 ¹⁷	4.2×10 ⁻⁸	-49.6	6
HDO	1.43	105	0.4×10 ¹⁷	1.5×10 ⁻⁸	-49.4	6
OCS	1.93	105	3.2×10 ¹⁷	1.2×10 ⁻⁷	-49.2	5
O ¹³ CS	1.93	105	0.04×10 ¹⁷	1.5×10 ⁻⁹	-49.1	5
HCN v ₂ =1	1.46	360	0.25×10 ¹⁷	9.6×10 ⁻⁹	-48.5	8
CH ₃ CN	1.37	55	0.15×10 ¹⁷	5.8×10 ⁻⁹	-47.2	6
	0.9	200	0.3×10 ¹⁷	1.2×10 ⁻⁸	-49.7	4
CH ₃ ¹³ CN	1.37	55	0.002×10 ¹⁷	7.7×10 ⁻¹¹	-47.2	4.5
	0.9	200	0.004×10 ¹⁷	1.5×10 ⁻¹⁰	-49.7	3
CH ₃ CN v ₈ =1	0.9	200	0.3×10 ¹⁷	1.2×10 ⁻⁸	-49.7	4
C ₂ H ₅ CN	1.93	105	0.08×10 ¹⁷	3×10 ⁻⁹	-48	7
¹³ CS	2.85	105	0.014×10 ¹⁷	5.4×10 ⁻¹⁰	-49.4	4
SO ₂	1.93	105	0.7×10 ¹⁷	2.7×10 ⁻⁸	-49.3	6
W3(OH)						
CH ₃ CN	2.2	95	0.016×10 ¹⁷	...	-46	5
CH ₃ OH	3.5	155	2.2×10 ¹⁷	...	-44.8	5
CH ₃ OCHO	3.8	95	0.4×10 ¹⁷	...	-44.7	5
OCS	2.7	95	0.25×10 ¹⁷	...	-44.3	5
¹³ CS	3.76	95	0.005×10 ¹⁷	...	-45.6	4.3
SO ₂	2.1	95	0.15×10 ¹⁷	...	-45.2	5.6

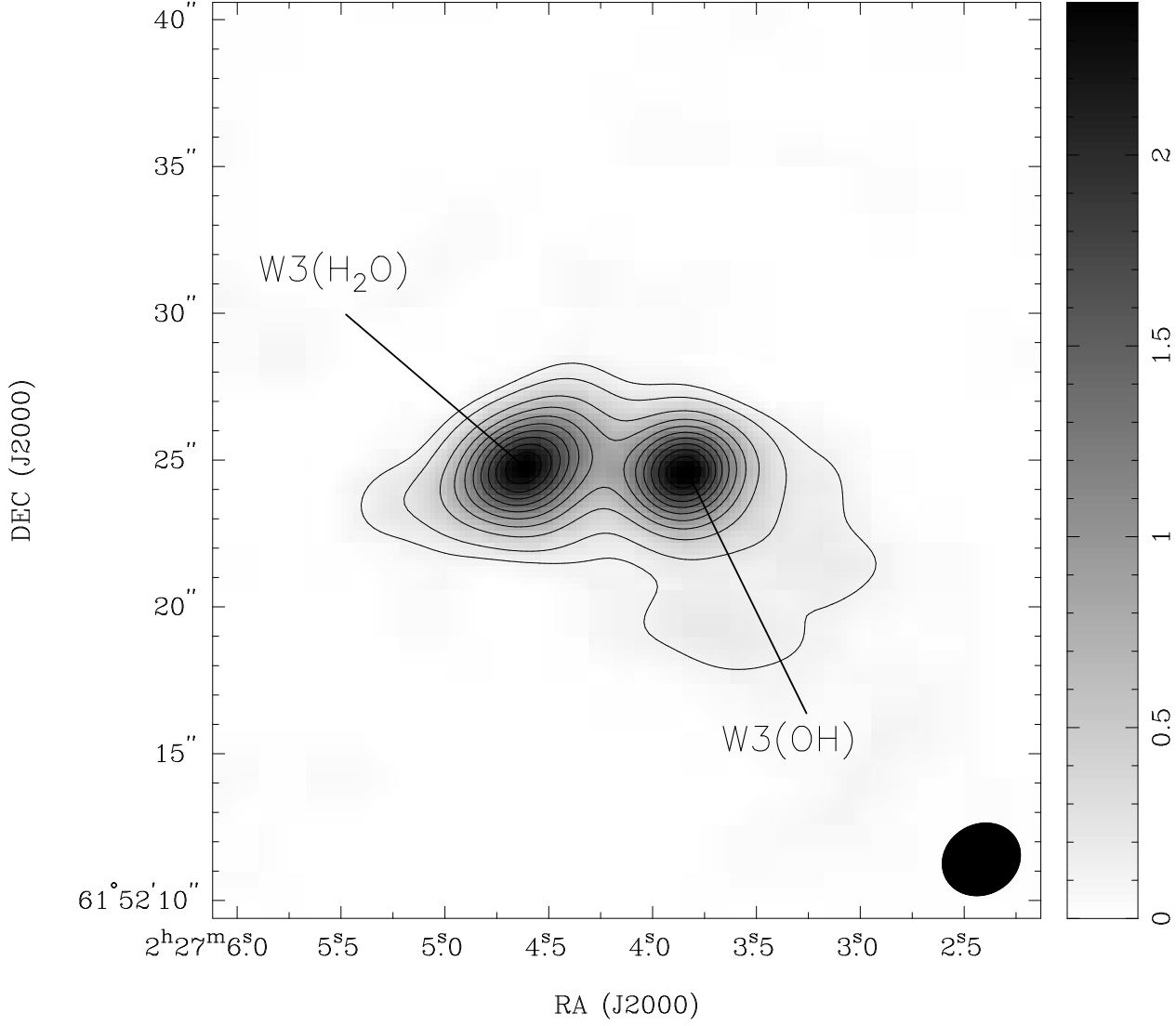


Fig. 1.— Continuum image of W3(OH) complex in both contours and grey scale. The contours are from 10 to 90% of the maximum intensity (2.3 Jy beam⁻¹). The synthesized beam of $\sim 2''.7 \times 2''.4$ (PA= -61°) is shown in lower right corner.

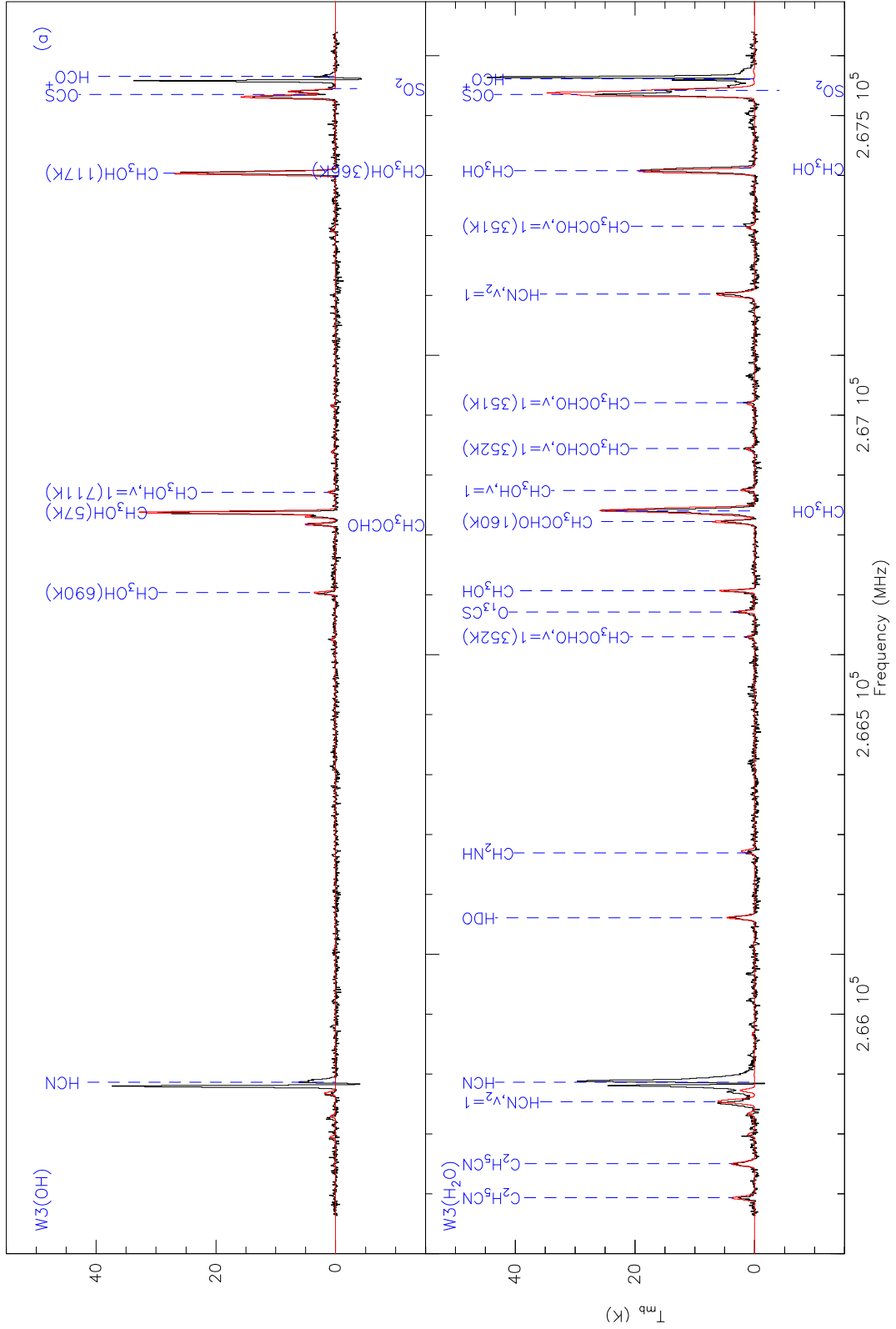


Fig. 2.— A: Lower sideband spectra at W3(H₂O) and W3(OH) continuum peak positions. The black curve is the observed spectral profile and red curve is from LTE modeling using XCLASS software. Upper panel is for W3(OH) and lower panel is for W3(H₂O). The upper level energies (E_u) of CH₃OH and CH₃OCHO are labelled. CH₃OH (9_{0,9}-8_{1,7}) and (17_{1,17}-16_{2,14}) at 267.4 GHz are blended together.



Fig. 2.— B: upper sideband spectra ($\text{CH}_3^{13}\text{CN}$ is not labelled in this figure) and XCLASS fitting. CH_3CN (15_0-14_2) and (15_1-14_1) at ~ 275.9 GHz are blended together. The upper level energy (E_u) of CH_3OCHO are labelled. U indicates the unidentified lines.

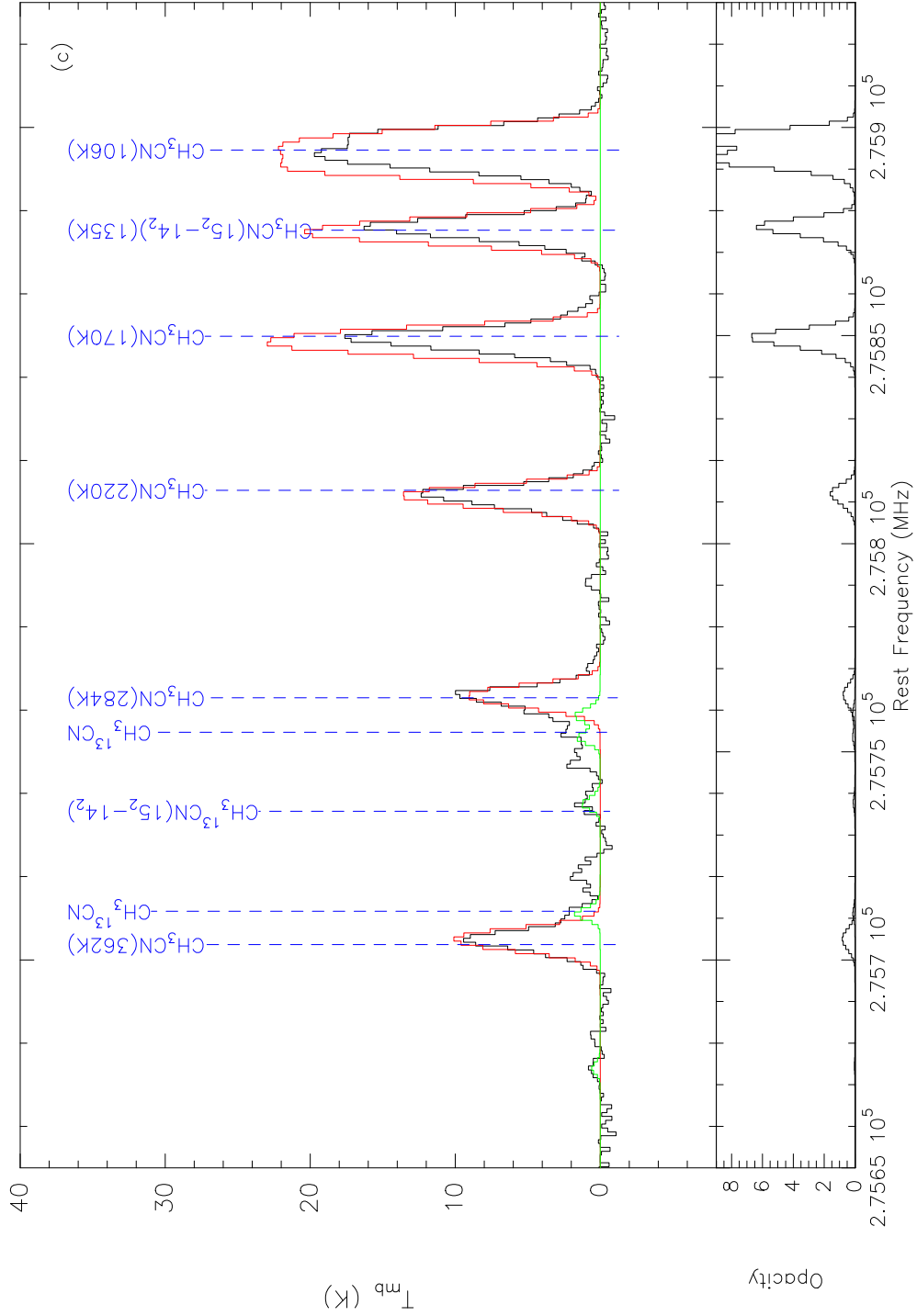


Fig. 2.— C: CH_3CN spectra and XCLASS fitting. In upper panel, the black curve indicates the observed spectrum, and red and green are the synthesized spectra for CH_3CN and $\text{CH}_3^{13}\text{CN}$), by use of both cold and warm components. In lower panel, the black curve is the calculated opacity. The upper level energy (E_u) of CH_3CN are labelled. CH_3CN (15_0-14_0) is blended with (15_1-14_1) at 275.91 GHz; $\text{CH}_3^{13}\text{CN}$ (15_0-14_0) is blended with (15_1-14_1) at 275.77 GHz.

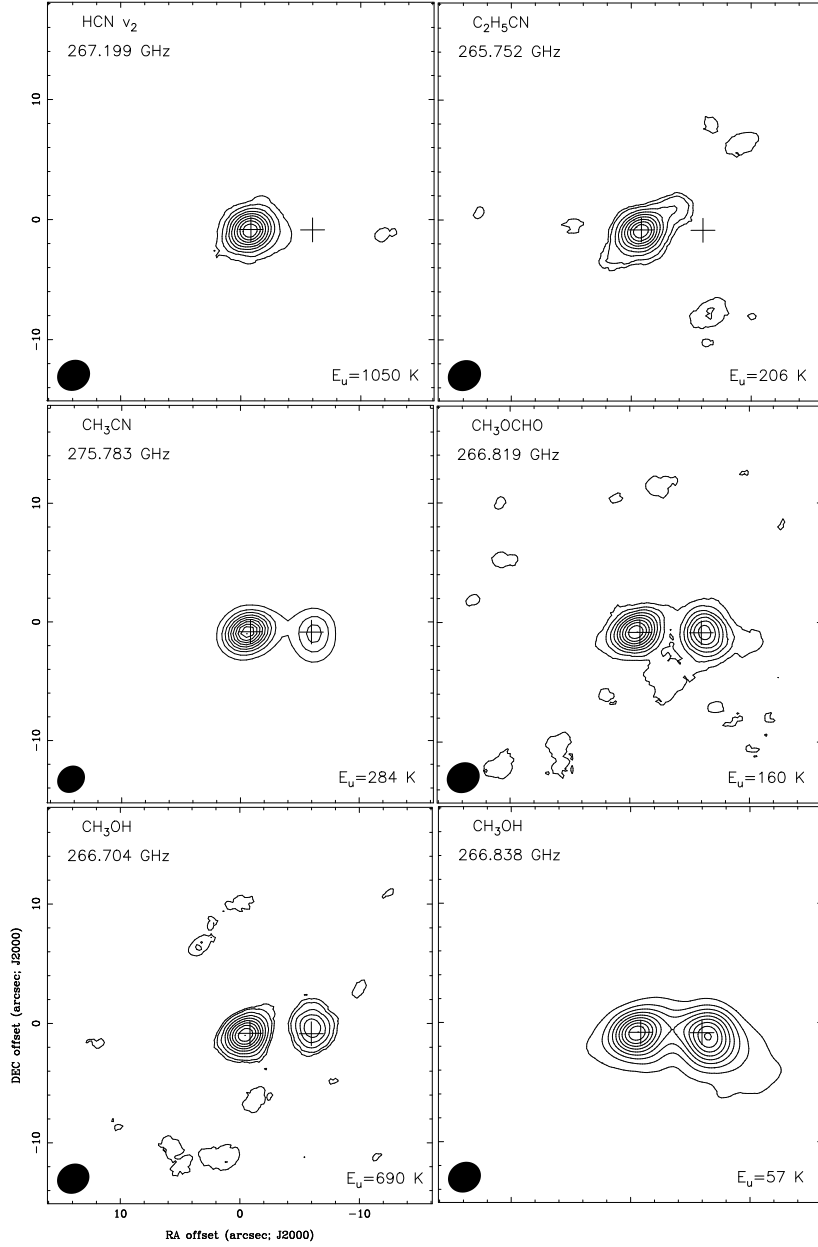


Fig. 3.— Sample images from specific molecular species. The contours are from 10 to 90% of the maximum integrated intensity for each molecular transition. The peak values of HCN v_2 , C_2H_5CN , CH_3CN , CH_3OCHO , higher and lower energy transitions of CH_3OH are 19.6, 11.6, 41.7, 12.2, 11.5, 78.5 Jy beam $^{-1}$ km s $^{-1}$, respectively. In each panel, the synthesized beam is shown in lower-left corner, and the cross symbol indicates the peak position of the continuum source.

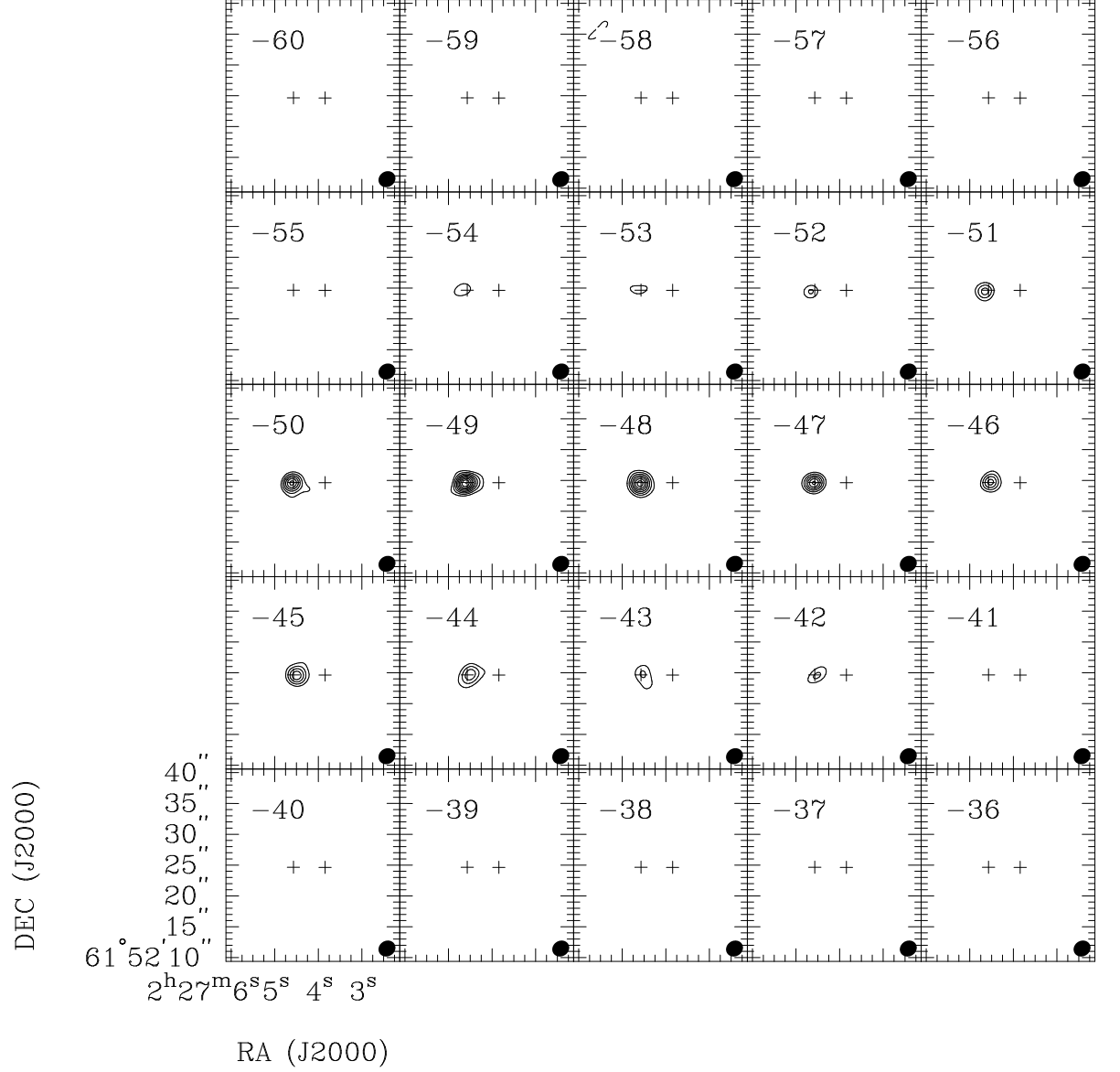


Fig. 4.— Channel maps of HCN $v_2=1$ at 267.199 GHz with FWHM beam size of $\sim 2''.7 \times 2''.4$, PA= -61° (lower right corner). The contours are from 10 to 90% of the peak intensity (2.3 Jy beam^{-1}). The rms (1σ) noise level is $0.09 \text{ Jy beam}^{-1}$. In each panel, the cross symbol indicates the peak position of the continuum source.

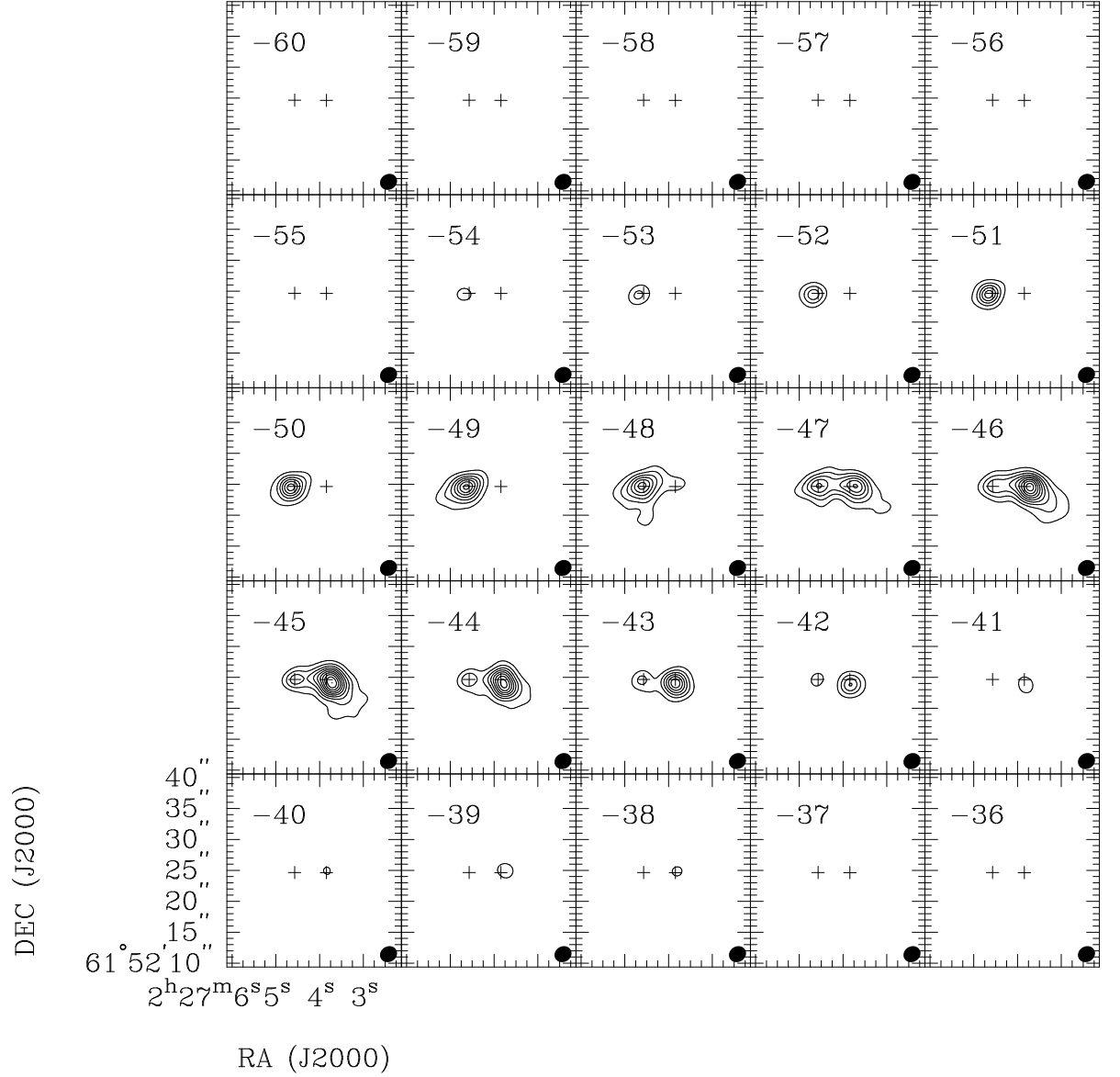


Fig. 4.— Continue: Channel maps of CH₃OH at 266.838 GHz with FWHM beam size of $\sim 2''.7 \times 2''.4$, PA= -61° (lower right corner). The contours are from 10 to 90% of the peak intensity ($14.2 \text{ Jy beam}^{-1}$). The rms (1σ) noise level is $0.11 \text{ Jy beam}^{-1}$. In each panel, the cross symbol indicates the peak position of the continuum source.

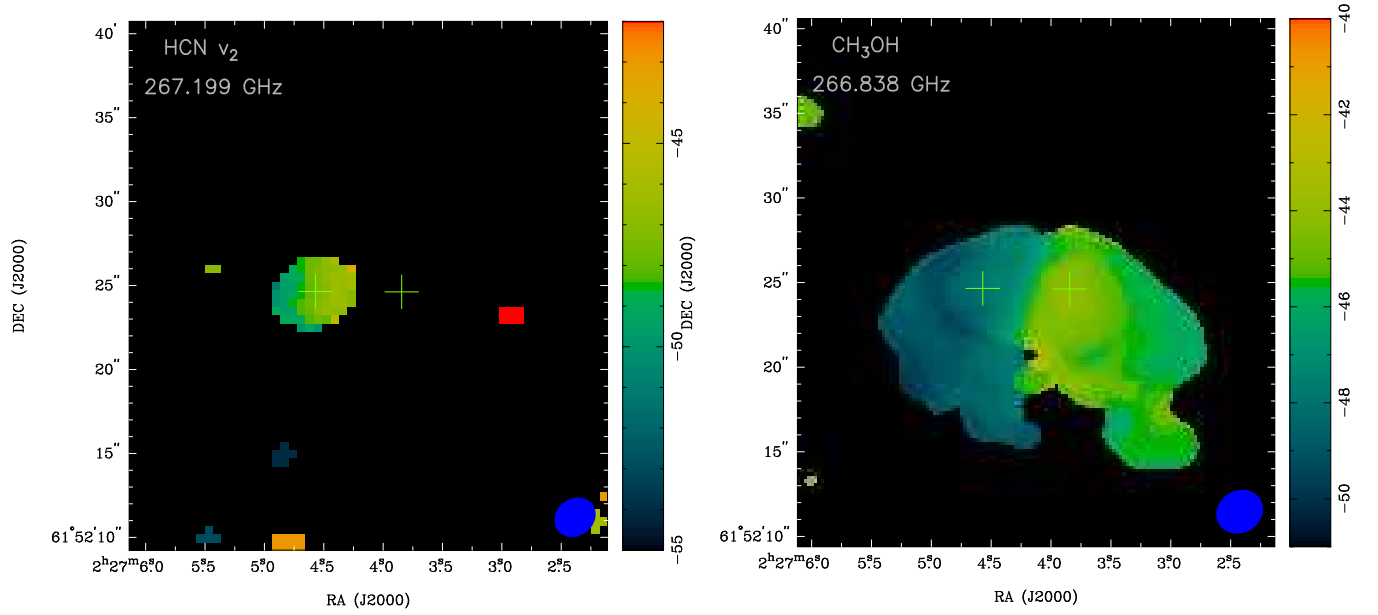


Fig. 5.— Intensity-weighted velocity maps of HCN $v_2=1$ at 267.199 GHz, and CH₃OH at 266.838 GHz with FWHM beam size of $\sim 2''.7 \times 2''.4$, PA= -61° . The scales on the right show the velocity range.

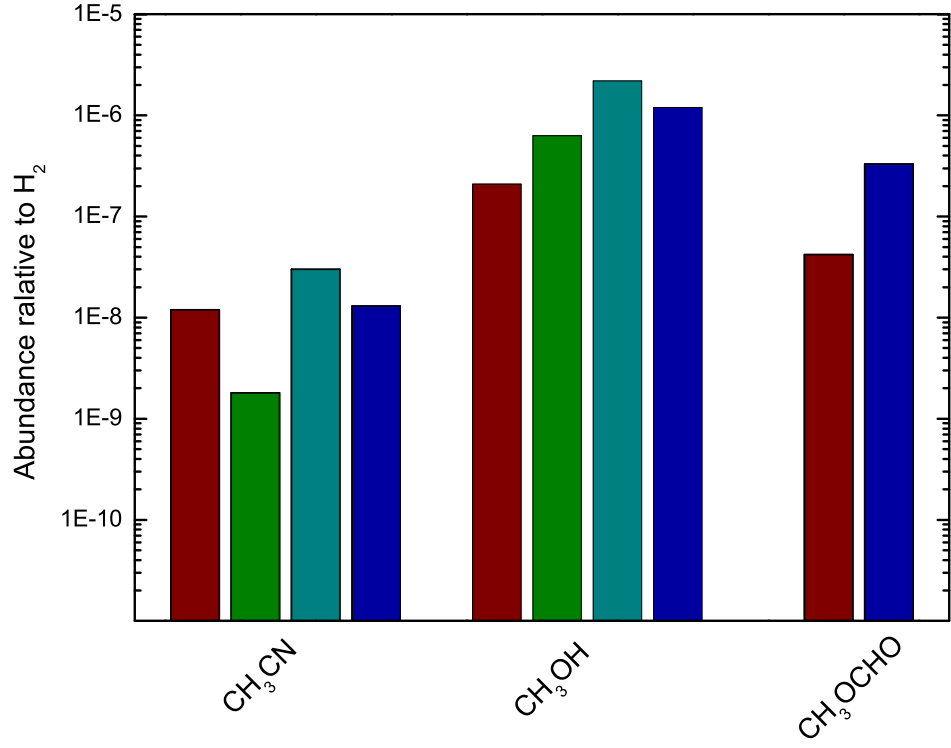


Fig. 6.— Abundances of molecules in W3(H₂O) relative to H₂ (maroon bars), compared to abundances in the Sgr B2(N) hot core (green) from Neill et al. (2014), the Orion KL Hot core (turquoise) and Compact Ridge (blue) from Crockett et al. (2014).